第 43 卷 第 19 期/2023 年 10 月/光学学报 研究论文

光学学报

少模光纤模式反射迈克尔孙干涉仪及其游标增敏应用

武瑞妮[1]，林国辉[2]，吕海飞[1]，黎敏[1]，李明钰[1]，王嘉赋[1]，文晓艳[1*]

[1]武汉理工大学理学院，湖北 武汉 430070；

[2]中兴通讯无线产品运营部，广东 深圳 518000

摘要 提出了一种少模光纤迈克尔孙干涉仪(MI)级联法布里-珀罗干涉仪(FPI)的游标增敏折射率传感器。少模光纤MI用作参考干涉仪，开放腔FPI作为传感干涉仪，解决了传统双FPI传感器的参考干涉仪制备复杂、可控性差的问题。仿真研究了单模-少模光纤错位量对少模光纤模式激发效率的影响，以及少模光纤长度对增敏倍数的影响。基于仿真优化参数制备了少模光纤MI-FPI传感器，并测试了其折射率响应特性，分析了增敏极限及限制因素。该传感器在1.3384～1.3412的折射率范围内的折射率灵敏度达到12466.956 nm/RIU(灵敏度单位)，相对于无MI级联的单个FPI传感器提升了12.29倍，放大倍数可基于少模光纤长度灵活控制。该方法使传感器的增敏效果显著、增敏倍数可控、制备方法简单且光谱稳定性好，在折射率传感领域具有潜在的应用价值。

关键词 光纤光学；迈克尔孙干涉仪；少模光纤；模式反射；游标效应；折射率传感器

中图分类号 O436 **文献标志码** A **DOI**：10.3788/AOS230520

1 引 言

折射率测量在生化分析、环境监测、食品安全等领域有着广泛的应用。光纤折射率传感器体积小、可实时在线监测、响应快，近年来得到了广泛的关注。典型的光纤折射率传感器包括光纤锥形传感器[1-2]、光纤等离子体共振传感器[3-6]、光纤光栅传感器[7-9]、光纤法布里-珀罗干涉仪(FPI)传感器等[10-11]，其中光纤FPI型传感器由于结构简单而引起了广泛关注。为提高灵敏度，学者们提出了将两个FPI单元干涉仪级联的游标增敏方法[12-15]。其中一个FPI用作传感干涉仪，另一个用作参考干涉仪，取得了明显的增敏效果。然而，双FPI游标增敏方法不仅要求两个单元干涉仪的自由光谱区范围(FSR)非常接近，同时还要求两者的光谱对比度均比较高、干涉成分稳定，以便级联后能获得明显的包络与增敏效果[16-17]。这对单元干涉仪的制作及级联均提出了较高要求。传统的FPI型参考单元干涉仪制作通常涉及到封闭腔体的加工，如将两段单模光纤插入一根毛细管然后用胶黏剂固化[18-19]，或者在两段单模光纤之间熔接一段微米量级的空心光纤[20]等。由于胶黏剂固化的不均匀性、空芯光纤切割设备要求高、端面切割不平整等原因，单元干涉仪的腔长及其FSR均难以控制，导致级联传感器的增敏可控性差。

线内光纤迈克尔孙干涉仪(MI)是反射式结构，集光的分束、传输与耦合为一体，不需要像FPI空腔制作那样进行端面对准，更易于加工和控制，并且也可与FPI级联进行增敏。目前常见的光纤MI是基于多模光纤、光子晶体光纤或细芯光纤制作[21-26]，含有多个模式，其输出光谱是不同模式间干涉的叠加，干涉成分繁多、光谱形状复杂，不利于追踪光谱变化。并且，由于模式难以控制，FSR的调控也较为困难。同时，模式数量的增加也引起能量分散，光谱对比度较低。

少模光纤(FMF)仅能传输有限的几个光纤模式，其干涉光谱仅含有限的几个模式，干涉成分简单、光谱形状规整，更有利于光谱解调、变化追踪与FSR调控。并且，由于模式数量减少，能量更为集中，大大提高了光谱对比度。此外，FMF的模式均在纤芯中传输，对外界折射率变化不敏感，其传输特性相对于多模光纤、光子晶体光纤、细芯光纤等的包层传输方式更为稳定，将其用作参考干涉仪更有利于提高传感器的稳定性。

本文构建了FMF MI作为参考干涉仪，将其与光纤FPI传感干涉仪级联用于折射率游标增敏。理论研究了FMF MI与FPI级联的增敏极限及其与测试系统光谱范围的关系，分析了MI腔长、单模-少模光纤错位量对增敏倍数的影响。基于理论优化结果，实验制备了FMF MI与FPI级联的游标增敏传感器，并测试了

收稿日期：2023-02-06；**修回日期**：2023-03-12；**录用日期**：2023-04-24；**网络首发日期**：2023-05-08

基金项目：国家自然科学基金(62075174，11974266)、中央高校基础研究基金(WUT2021Ⅲ063JC)

通信作者：*wenxy@whut.edu.cn

其折射率响应特性。该传感器在1.3384～1.3412的折射率范围内的折射率灵敏度达到12466.956 nm/RIU(灵敏度单位),相对于无MI级联的单个FPI传感器提升了12.29倍。该方法使传感器的增敏效果显著、制备方法简单、光谱稳定性好,在折射率传感领域具有潜在的应用价值。

2 理论分析与仿真

2.1 FMF MI的游标增敏原理

光学游标效应一般由两个FSR接近但不完全相等的干涉仪级联形成,其中对待测量不敏感的干涉仪一般作为参考干涉仪,用于对传感干涉仪进行游标增敏。光纤的纤芯模式在纤芯内传输,不易受外界折射率变化的影响,对外界折射率变化几乎不敏感,因此可将基于纤芯模式传感的FMF MI结构作为参考干涉仪。本文设计了单模-少模错位熔接的FMF MI传感器,其结构示意图如图1所示。

图中包括输入单模光纤(SMF)和FMF,光由SMF输入至SMF-FMF熔接点处时,由于模场不匹配,FMF中不同光纤模式被激发,并沿FMF传输,至FMF端面时被反射。当反射光传回至SMF-FMF熔接点处时会合束,并发生干涉。其光谱I_R的表达式为

$$I_R = I_{01} + I_{11} + 2\sqrt{I_{01}I_{11}}\cos\left(\frac{4\pi L_R}{\lambda}\Delta n_{eff}\right) = A_R + B_R\cos\varphi_R, \tag{1}$$

式中:L_R表示MI的腔长(即FMF长度);I_{01}和I_{11}分别为LP_{01}和LP_{11}两模式的光强;Δn_{eff}为两模式的有效折射率差;$\varphi_R = \frac{4\pi L_R}{\lambda}\Delta n_{eff}$为两模式的干涉相位差;$A_R$和$B_R$分别表示直流项和交流项的幅值。

光纤FPI折射率传感器的灵敏度较高,在1.33～1.35折射率变化范围内,灵敏度约为1100 nm/RIU,可将其作为传感干涉仪。FPI结构示意图如图2所示,其原理为:LP_{01}和LP_{11}模式从FMF的M_1面出射进入FPI,在FPI腔中传输,到达FPI的M_2面时被反射,返回至M_1面时与M_1面的反射光合束并干涉。干涉的光程差为$2nL_S$,其中n为FPI腔内介质的折射率,L_S为FPI的腔长。LP_{01}和LP_{11}模式离开光纤进入FPI腔后,由于FPI腔不是光纤波导,模式理论不适用,具体传输过程有待进一步理论研究。本文简化处理,将M_2面的反射光视为一束光I_b,对应将M_1面的反射光视为一束光I_a。则干涉光谱I_S的表达式为

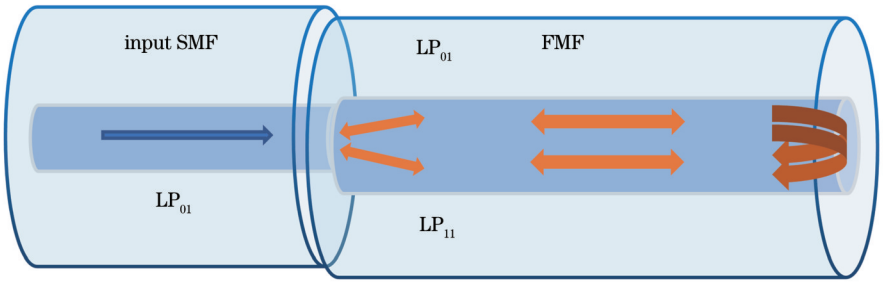

图1 FMF MI的结构示意图

Fig. 1 Structural diagram of FMF MI

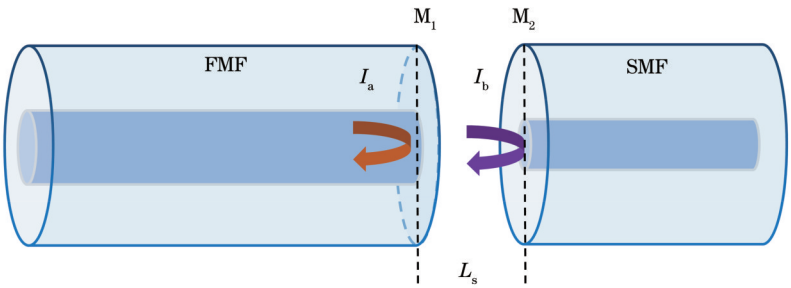

图2 FMF-SMF FPI的结构示意图

Fig. 2 Structural diagram of FMF-SMF FPI

$$I_S = I_a + I_b + 2\sqrt{I_a I_b}\cos\left(\frac{4\pi n L_S}{\lambda}\right) = A_S + B_S\cos\varphi_S, \tag{2}$$

式中:L_S表示开放腔FPI的腔长(即传感干涉仪腔长);n表示腔内介质的折射率;$\varphi_S = \frac{4\pi n L_S}{\lambda}$为$I_a$和$I_b$的干涉相位差;$A_S$和$B_S$分别表示直流项和交流项的幅值。

将MI与FPI级联后,级联干涉仪的传感系统及结构示意图如图3所示。传感器包含输入SMF、FMF、开放腔FPI以及末端SMF四个部分,其中开放腔FPI两端的光纤用紫外固化胶(UV glue)固定在载玻片上。

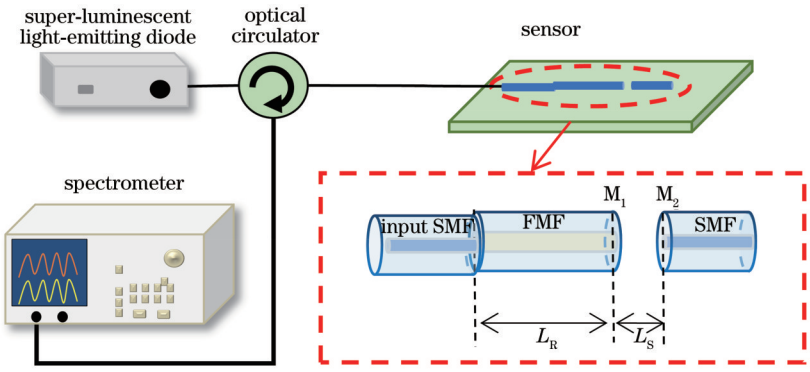

图 3 传感器及系统结构示意图

Fig. 3 Structure diagram of sensor and system

以 LP_{01}-LP_{11} 模式的传输与干涉为例进行分析(如图 1 所示)。LP_{01}、LP_{11} 两模式在 SMF-FMF 熔接点处被激发,传输至反射面 M_1 时,部分光被反射并沿 FMF 反向传输至 SMF−FMF 熔接点处干涉,此为 MI 干涉。同时,M_1 处也有透射光进入 FPI 腔中传输,至反射面 M_2 时被反射,再经 FPI 传输后进入 FMF,与 M_1 面的反射光干涉,此为 FPI 干涉。传感器输出光谱是两个单元干涉仪光谱的叠加。本文将 FMF MI 作为参考干涉仪,FPI 作为传感干涉仪,用 I_R 和 I_S 分别表示参考干涉仪和传感干涉仪的光强。级联光谱表现为两个干涉的叠加,其干涉光谱为两单元干涉仪光强相乘[27],如下式所示:

$$I = I_S I_R。\tag{3}$$

将式(1)和式(2)代入式(3)可得

$$I = A_R A_S + A_S B_R \cos\varphi_R + A_R B_S \cos\varphi_S + 0.5 B_R B_S \cos(\varphi_S + \varphi_R) + 0.5 B_R B_S \cos(\varphi_S - \varphi_R),\tag{4}$$

式中的低频分量 $\varphi_S - \varphi_R$ 决定了级联谱的包络[28]。

2.2 FMF 中的模式求解与模式激发效率仿真

本文所用的 FMF 为长飞公司生产的四模光纤,纤芯、包层直径分别为 18.5、125.0 μm,纤芯、包层折射率分别为 1.450、1.444,支持 LP_{01}、LP_{11}、LP_{21} 和 LP_{02} 四种模式传输。首先,基于上述光纤参数计算得到各模式在不同波长下的有效折射率如图 4(a)所示。

为在 MI 中获得特定模式的干涉,需要对 FMF 的模式激发进行控制。SMF 与 FMF 错位熔接时,错位量会影响 FMF 中模式的激发效率。因此调节错位量便可调控 FMF 模式的激发效率,从而调控参与干涉的模式成分。首先理论计算了不同 SMF-FMF 错位量下 FMF 模式的激发效率。本文选择纤芯尺寸较为适中的四模光纤,以便错位时大部分光仍能进入 FMF 的纤芯传输,从而降低包层模式的激发效率,减少干涉成分和包层模式的干扰。根据 SMF 和 FMF 错位熔接的重叠积分,得到错位下的激发效率[29]为

$$\eta = \frac{\left|\int_0^\infty E_{SMF}(r) E_{FMF}(r) r\mathrm{d}r\right|^2}{\int_0^\infty \left|E_{SMF}(r)\right|^2 r\mathrm{d}r \int_0^\infty \left|E_{FMF}(r)\right|^2 r\mathrm{d}r},\tag{5}$$

式中,E_{SMF} 和 E_{FMF} 分别表示 SMF 和 FMF 的光场,其中错位时的 SMF 入射光场可以表示为

$$E_{SMF} = \exp\left(-\frac{r^2 + 2r\cos\theta \cdot \Delta x + \Delta x^2}{w_g^2}\right) \cdot \exp(-i\beta_0 z) \cdot \hat{x},\tag{6}$$

式中:r 表示 SMF 的半径;w_g 为高斯光束的半峰全宽(FWHM);β_0 为基模传播常数;Δx 表示沿 x 轴方向的偏移量。根据式(6)可以计算得到不同单模-四模错位量下各模式的激发效率,如图 4(b)所示。在 2~5 μm 错位范围内,LP_{01} 和 LP_{11} 模式的激发效率都相对较高也较为接近[图 4(b)阴影部分]。在错位量为 5~9 μm 的范围内,LP_{21} 模式的激发效率最高,LP_{11} 和 LP_{01} 次之且较为接近。本文综合考虑模式激发效率及传感器机械强度要求,通过多次实验优化,最终确定 SMF-FMF 的错位量为 3 μm,激发的主要是 LP_{01} 和 LP_{11} 模式。

2.3 FMF MI 的增敏极限及其腔长控制

FMF MI 与传感 FPI 级联传感器的放大倍数由两个单元干涉仪的 FSR 决定[27],如下式所示:

$$M = \frac{F_{SRR}}{\left|F_{SRS} - F_{SRR}\right|},\tag{7}$$

式中:F_{SRR} 表示参考干涉仪的 FSR;F_{SRS} 表示传感干涉仪的 FSR。对光谱做快速傅里叶变换(FFT)后可得各干涉成分的空间频率 ξ,且 $\xi = \frac{1}{F_{SR}}$。则游标放大倍数可表示为

$$M = \frac{\xi_S}{\left|\xi_R - \xi_S\right|},\tag{8}$$

式中:ξ_S 表示传感干涉仪的空间频率;ξ_R 表示参考干涉仪的空间频率;$\left|\xi_R - \xi_S\right|$ 为游标增敏后包络的空间频率。

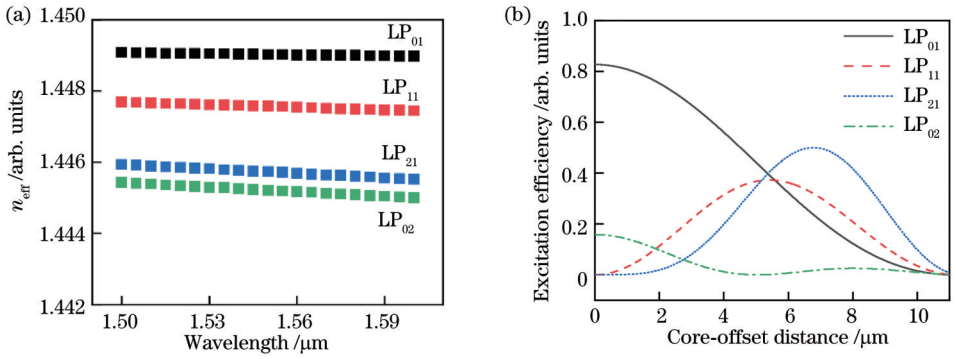

图4 FMF模式的有效折射率及错位量对模式激发效率的影响。(a) FMF模式的有效折射率;(b) 不同SMF-FMF错位量下各模式的激发效率

Fig. 4 Effective refractive index of modes in FMF and effect of core-offset on mode excitation efficiency. (a) Effective refractive indexes of modes in FMF; (b) excitation efficiency of modes under different core-offsets in SMF-FMF

根据式(8),理论上只要$|\xi_R-\xi_S|$无限小,M便可以无限大。然而,实际上$|\xi_R-\xi_S|$的值受限于探测光谱宽度。本文所用的宽谱光源为超发光二极管(SLED),中心波长约为1550 nm,光源的FWHM约为100 nm。用光谱仪(YOKOGAWA, AQ6370)探测1500~1600 nm波长范围的干涉光谱,然后对干涉光谱做FFT得到其空间频率谱。空间频率谱的频率分辨率即可以被分辨的最小频率间隔可表示为

$$\Delta Rw=\frac{1}{T}=0.01\ \mathrm{nm}^{-1}, \tag{9}$$

式中,T表示信号的长度,即光谱仪探测的波长范围(100 nm)。所以对应的空间频率谱分辨率为0.01 nm^{-1},即$|\xi_R-\xi_S|$的理论最小值为0.01 nm^{-1}。然而,为便于波长追踪,在100 nm的光谱范围内最少需要有2个完整的包络,即包络的最大FSR为50 nm,故$|\xi_R-\xi_S|$的最小值应为0.02 nm^{-1}。

根据式(8),$|\xi_R-\xi_S|$最小值一定的情况下,游标效应的放大倍数与ξ_S有关。理论上ξ_S越大,放大倍数越高。对于FPI型传感干涉仪,由$\xi=\frac{1}{F_{SR}}$,$F_{SR}=\frac{\lambda^2}{2nL_S}$两式可知,$\xi_S$越大则所需腔长$L_S$越长,不利于传感器结构的小型化,因此需要综合考虑放大倍数和传感器尺寸需求,合理设置L_S。本文拟实现一个数量级以上的增敏效果,因此只需ξ_S为0.2 nm^{-1}即可。实验时根据该值制备FPI,测量得到其实际的FSR及ξ_S,再依据ξ_S及放大倍数要求计算得到参考干涉仪的理论FSR及ξ_R值,算出MI腔长理论值,再据此进行MI的制作及其与FPI的级联。

本文待测折射率测量范围为1.3384~1.3412,在此折射率范围内普通FPI折射率传感器的灵敏度约为1100 nm/RIU,对应的波长漂移量大于3 nm。为便于追踪同一波谷的折射率响应,干涉光谱的FSR需大于3 nm。另外根据式(8)及上一段的分析结果,对于0.02 nm^{-1}的$|\xi_R-\xi_S|$,当ξ_S大于0.2 nm^{-1}(即传感干涉仪的FSR小于5 nm时),理论放大倍数可达10倍以上。综上考虑,本文选择FSR为4 nm左右的传感干涉仪进行FPI的制作。实验制作的FPI单元干涉仪的干涉光谱及空间频率谱如图5所示,其FSR为4.12 nm,对应的空间频率ξ_S为0.24 nm^{-1},腔长约为215.4 μm。

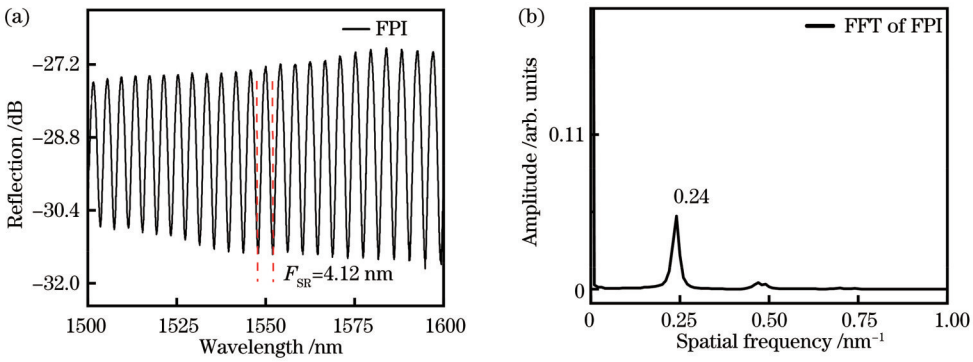

图5 FPI的干涉光谱及其空间频率谱。(a)干涉光谱;(b)空间频率谱

Fig. 5 Interference spectrum of FPI and its spatial frequency spectrum. (a) Interference spectrum; (b) spatial frequency spectrum

如前所述，对于ξ_S为0.24 nm^{-1}的传感干涉仪，要获得最大的放大倍数，参考干涉仪的空间频率ξ_R应为0.22 nm^{-1}或0.26 nm^{-1}。由于较小的ξ_R对应较短的FMF长度，为减小传感器尺寸，本文选择0.22 nm^{-1}为理论ξ_R进行分析，对应MI的FSR约为4.55 nm。基于该参数对MI的腔长进行仿真，从而为MI的制作提供参考。

由式(1)可知，当$\varphi=(2m+1)\pi$ ($m=0, \pm1, \pm2, \cdots$)时，MI干涉光谱出现干涉极小。第m阶极小对应的波谷为

$$\lambda_m=\frac{2\pi\Delta n_{\mathrm{eff}_m}L}{(m+1)\pi}。\tag{10}$$

两相邻波谷之差(即FSR)可表示为

$$F_{\mathrm{SR}}=\lambda_m-\lambda_{m-1}=\frac{2\pi\Delta n_{\mathrm{eff}_m}L}{(m+1)\pi}-\frac{2\pi\Delta n_{\mathrm{eff}_m-1}L}{(m-1)\pi},\tag{11}$$

式中，$\Delta n_{\mathrm{eff}_m}$和$\Delta n_{\mathrm{eff}_m-1}$分别是波谷$\lambda_m$和$\lambda_{m-1}$对应的折射率(考虑色散)。

基于上述公式并结合图4(a)的数据，对不同FMF长度下LP_{01}-LP_{11}模式干涉的光谱进行仿真，结果如图6所示。由图可知，LP_{01}-LP_{11}干涉谱的FSR随FMF长度增加而减小。当FMF长度为30 cm时，干涉光谱FSR接近4.55 nm。在30 cm的基础上进一步优化，得知当FMF长度为31.6～33.0 cm时，空间频率均为0.22 nm^{-1}。在该范围内，以0.1 cm为步长改变FMF的长度，构造出MI仿真信号与FPI的实验信号叠加，对游标增敏效果进行比较。

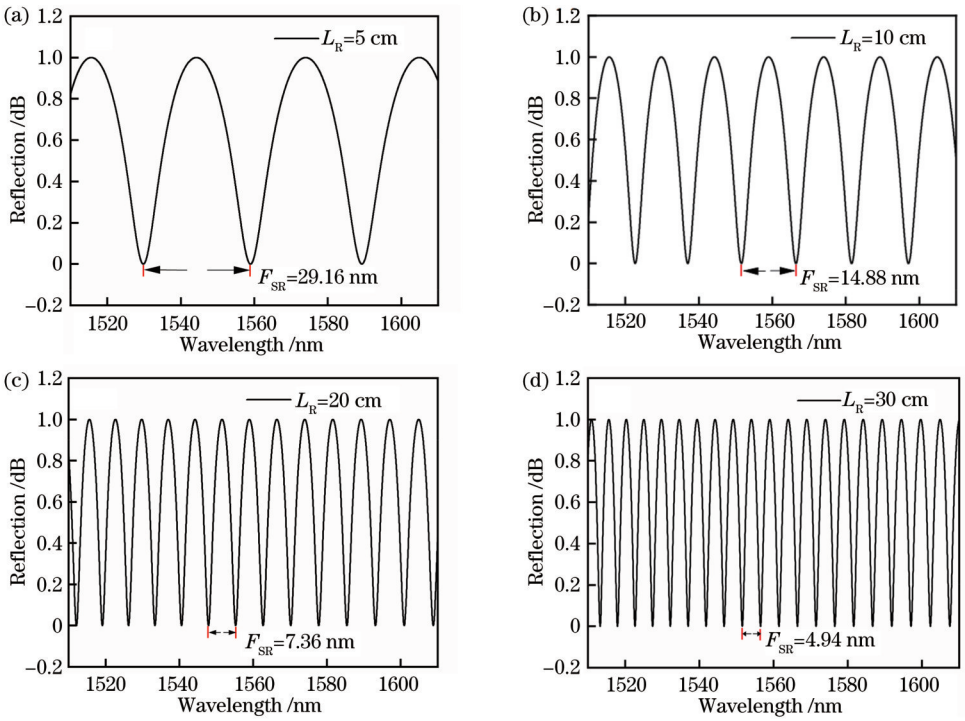

图6 不同L_R的MI干涉光谱图。(a) L_R=5 cm；(b) L_R=10 cm；(c) L_R=20 cm；(d) L_R=30 cm

Fig. 6 Interference spectra of MI with different L_R. (a) L_R=5 cm; (b) L_R=10 cm; (c) L_R=20 cm; (d) L_R=30 cm

MI仿真信号虚拟游标解调具体步骤为：首先对实验制备的FPI单元干涉仪进行不同折射率溶液的响应测试。测试了质量浓度范围为2%～4%、质量浓度间隔约为0.5%的NaCl溶液的折射率，各溶液折射率经阿贝折光仪进行标定，分别为1.3384、1.3390、1.3396、1.3405、1.3412。图7(a)为FPI的波长-折射率响应图，其波长-折射率灵敏度拟合结果如图7(f)中实线所示，单元FPI干涉仪的折射率灵敏度为1014.59 nm/RIU。然后将每个折射率下的FPI光谱与构造的MI信号[图7(b)]相乘，即可得到含有游标包络的级联光谱，如图7(c)所示。对其做傅里叶变换可得到级联光谱对应的空间频率谱，如图7(d)所示，图中所标示的频率峰由高到低依次为FPI、MI、级联包络的空间频率。提取包络的空间频率并将其做傅里叶逆变换[30]，即可得到级联的包络谱，如图7(e)所示。对各折射率溶液下包络谱的波长漂移进行拟合即可得到级联增敏后的灵敏度[图7(f)]。优化结果表明，当FMF长度为32.4 cm时，增敏倍数最大，折射率灵敏度达到12413.722 nm/RIU[图7(f)中虚线所示]，相对于单元FPI提升了12.24倍。

值得指出的是，32.4 cm的FMF长度不利于传感器的小型化。然而，根据式(11)可知，MI光谱的FSR除了与L_R有关外，还与模式有效折射率差Δn_{eff}有关，因此后期可合理设计FMF结构参数，增大Δn_{eff}，从而在同样的FSR需求下减小L_R，减小传感器尺寸。

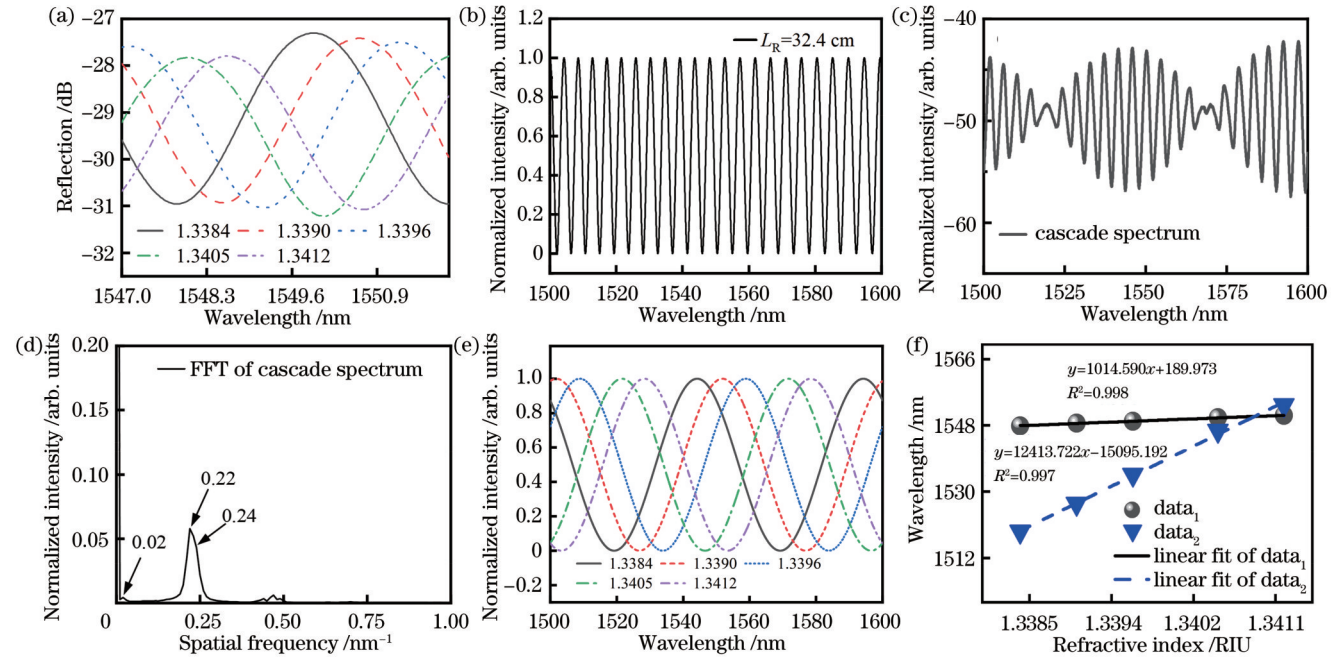

图 7 MI仿真信号游标解调结果图。(a)FPI折射率响应;(b)仿真MI干涉光谱;(c)级联光谱;(d)级联干涉仪空间频率谱;(e)级联干涉仪折射率响应;(f)MI游标增敏前后灵敏度拟合

Fig. 7 Vernier demodulation results of MI simulated signal. (a) Refractive index response of FPI; (b) interference spectrum of simulation MI; (c) cascade spectrum; (d) spatial frequency spectrum of cascade interferometer; (e) refractive index response of cascade interferometer; (f) sensitivity fitting with and without MI vernier sensitization

3 传感器结构参数优化与制作及折射率传感测试

实验时首先进行单元FPI的制作,过程如下:将FMF(长度大于32.4 cm)和SMF用切割刀切割,然后放在光纤熔接机上观察断面切割角度,小于1°则满足需求。然后用光纤研磨机研磨两个光纤切割端面使其更加平整。将研磨后的FMF和SMF固定在微位移平台的两端,并在光纤下方放置载玻片,在载玻片上滴注足量初始浓度的NaCl溶液(能够完全填充FPI开放腔)。通过微位移平台调控FMF和SMF反射面之间的距离,以调控FPI的腔长。基于前述理论分析结果,调控微位移平台使FPI的干涉谱的FSR至目标值附近(腔长约为215.4 μm)。用紫外固化胶分别将两段光纤与下方载玻片固定,然后用去离子水清洗载玻片并干燥FPI腔。胶黏固化的不均匀性可能会引起传感干涉仪腔长发生微小变化(ξ_S相应变化),一方面可以通过少量多次滴加紫外固化胶来进行改进。另一方面,由式(8)可知,游标增敏效果跟ξ_S和ξ_R有关。后期级联时,可以先测定固化后的ξ_S,然后通过调节ξ_R(即L_R)来匹配ξ_S,以获得理想的增敏效果。将制备好的FPI进行折射率传感测试,图7(a)为FPI的波长-折射率响应图,其波长-折射率灵敏度拟合结果如图7(f)中实线所示,实验结果表明,单元FPI的折射率灵敏度为1014.59 nm/RIU。

然后根据前述仿真结果进行MI的制作及其与FPI的级联。对远离FPI的FMF一端进行切割,使FMF长度为32.4 cm,再将其与入射SMF错位熔接,则形成了单元MI。具体熔接方法是将光纤熔接机(Fujikura FSM-60S)的熔接模式调整为手动模式,然后沿x轴调节驱动马达,使FMF与入射SMF的错位量为3 μm。测得MI的光谱如图8(a)中插图所示,其FFT谱中主峰的空间频率为0.22 nm^{-1}。其他模式干涉的能量很弱,可以忽略。实验测得的空间频率与前述仿真中32.4 cm FMF长度下LP_{01}-LP_{11}干涉的空间频率一致,说明MI为LP_{01}、LP_{11}两模式的干涉。

接下来进行MI-FPI的级联以及复合干涉仪的折射率传感性能测试,在实验过程中保持温度恒定。级联传感器的光谱及空间频率谱如图8(b)所示,光谱呈现了明显的包络。FFT谱中0.02 nm^{-1}的峰对应于包络的空间频率。对各折射率下的光谱进行处理,提取其包络对应的低频峰并进行傅里叶逆变换,得到图8(c)所示的响应图。对其进行拟合得到MI-FPI复合干涉仪的折射率灵敏度为12466.956 nm/RIU[图8(d)中虚线所示],相对于无MI增敏的单元FPI[图8(d)中实线所示]提升了12.29倍。

实际的增敏倍数与理论值存在一定的偏差,可能的原因是:第一,本文采用傅里叶逆变换法进行包络提取,适用于余弦信号的分析,然而由于实际MI的光谱并不是规整的余弦谱,导致短波长处的FSR小于长波长的FSR,故放大倍数存在一定偏差;第二,实验制备

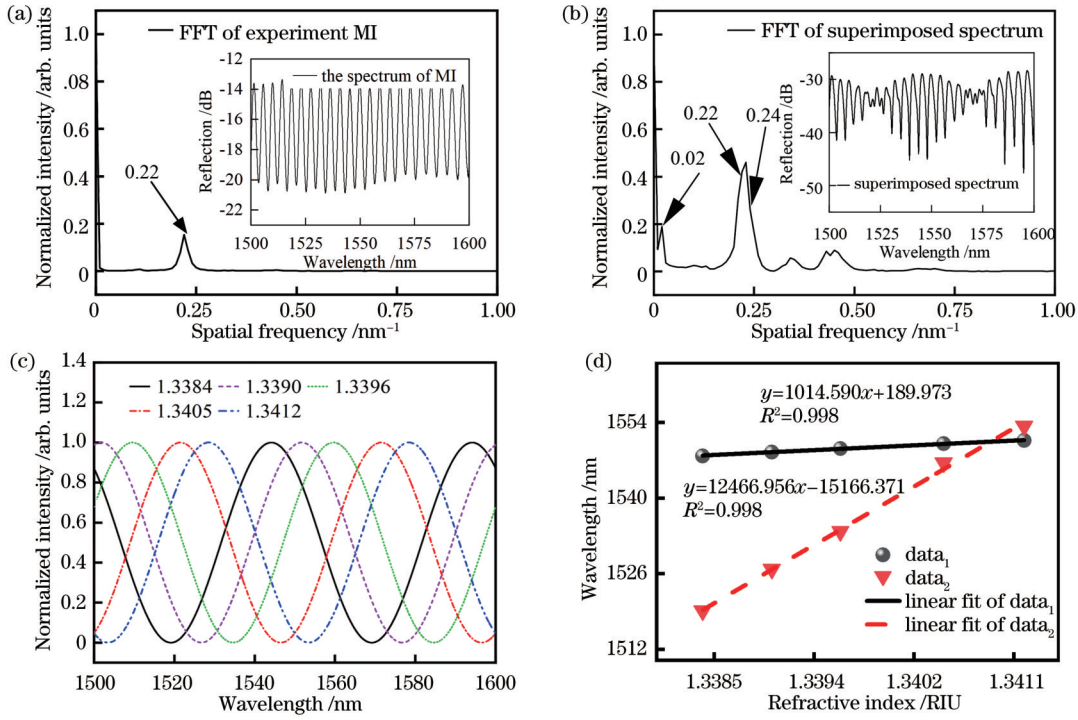

图 8 MI-FPI复合干涉仪折射率响应测试结果。(a) MI干涉光谱及空间频率谱;(b) MI-FPI干涉光谱及空间频率谱;(c) MI-FPI折射率响应谱;(d)游标增敏前后灵敏度拟合

Fig. 8 Refractive index response test results of MI-FPI composite interferometer. (a) Interference spectrum and spatial frequency spectrum of MI; (b) interference spectrum and spatial frequency spectrum of MI-FPI; (c) refractive index response of MI-FPI; (d) sensitivity fitting with and without MI vernier sensitization

MI时,FMF的长度控制存在误差,会导致ξ_R有一定误差,也会引起放大倍数产生偏差。结合2.3节有关增敏极限的分析,该传感器的灵敏度有望进一步提升,主要有两种途径:一是选用光谱范围更宽的光源来降低$|\xi_R-\xi_S|$最小值;二是增大FPI的腔长L_S来增大ξ_S。

值得注意的是,严格来讲,直接将FPI的干涉光谱做FFT,其光谱中包含了FPI腔长的信息,或者说,同一干涉光谱在不同波长处的FSR是不一样的(即短波长处FSR小于长波长处的FSR),对波长域干涉光谱直接做傅里叶变换会存在一定的误差。如果将干涉光谱的横坐标改成光波频率,其干涉光谱则在全波段具有相同的FSR,其大小只与参与干涉光束的光程差有关。然而,本文整个干涉光谱的波长范围不是很大(100 nm),即短波长处FSR与长波长处的FSR偏差很小。详细分析表明(过程略),直接对波长域光谱进行傅里叶变换,与转换到频率域插值后再做傅里叶变换,这两种处理方法的结果区别不大。故本文沿用了大多数文献处理包含多干涉模式光谱的一种常用方法,即对波长域干涉光谱直接做傅里叶变换[30-32]。若光谱的波长范围较大,则应将波长域光谱转换到频率域再插值,然后进行傅里叶变换,以减少腔长的偏差。

4 结 论

本文构建了FMF MI用作参考干涉仪,将其与用作传感干涉仪的光纤FPI级联用于折射率游标增敏。理论研究了FMF MI与FPI级联的增敏极限及其与测试系统光谱范围的关系,分析了MI腔长、SMF-FMF错位量对增敏倍数的影响。基于理论优化结果,实验制备了FMF MI与FPI级联的游标增敏传感器,并测试了其折射率响应特性。该传感器在1.3384~1.3412折射率范围内的折射率灵敏度达到12466.956 nm/RIU,相对于无MI级联的单元FPI传感器提升了12.29倍,增敏效果显著。

本文制备的FMF MI主要为纤芯模式的干涉,干涉成分稳定且具有较高的光谱对比度,适合作为参考干涉仪与其他干涉仪级联来实现游标增敏,可以根据需要与各种类型的FPI或其他干涉仪级联,如与膜片式FPI级联可以实现静压力、温度等物理量的游标增敏传感,也可直接在MI末端涂覆温敏或者湿敏材料构成FPI腔用于温度、湿度增敏传感等。本文基于FMF MI进行游标增敏的方法简单巧妙、传感器易于加工制作、成本低廉,且光谱可控性强、普适性高,在光纤传感领域具有广泛的应用前景。

参 考 文 献

[1] Zhang W H, Gao W L, Tong Z R, et al. Mach-Zehnder interferometer cascaded with FBG for simultaneous measurement of RI and temperature[J]. Optics Communications, 2020, 466: 125624.

[2] Gao W L, Zhang W H, Tong Z R, et al. Refractive index and

temperature sensor based on optical fiber Mach-Zehnder interferometer with trapezoid cone[J]. Optical Engineering, 2019, 58(5): 057102.

[3] 赵华新, 蒋永翔, 罗天穹, 等. 基于表面等离子体共振原理的空芯光纤传感器[J]. 光学学报, 2012, 32(6): 0628001.
Zhao H X, Jiang Y X, Luo T Q, et al. Hollow optical fiber sensor based on surface plasmon resonance[J]. Acta Optica Sinica, 2012, 32(6): 0628001.

[4] 范雨艳, 施伟华. 基于表面等离子体共振的光子晶体光纤生物传感[J]. 激光与光电子学进展, 2021, 58(21): 2106003.
Fan Y Y, Shi W H. Photonic crystal fiber biosensors based on surface plasmon resonance[J]. Laser & Optoelectronics Progress, 2021, 58(21): 2106003.

[5] Mumtaz F, Roman M, Zhang B H, et al. A simple optical fiber SPR sensor with ultra-high sensitivity for dual-parameter measurement[J]. IEEE Photonics Journal, 2022, 14(5): 6852907.

[6] Zhou Y N, Yan X. D-shaped fiber surface plasmon resonance refractive index sensor enhanced by MXene ($Ti_3C_2T_x$)[J]. IEEE Photonics Journal, 2022, 14(5): 7151607.

[7] Zou T, Zhong J L, Liu S, et al. Helical intermediate-period fiber grating for refractive index measurements with low-sensitive temperature and torsion response[J]. Journal of Lightwave Technology, 2021, 39(20): 6678-6685.

[8] Wen H Y, Lee K N, Hsu Y C, et al. Sensors in tilted fiber Bragg gratings via spherical metal-reflective ends[J]. IEEE Sensors Journal, 2021, 21(3): 2989-2994.

[9] Mizuno Y, Theodosiou A, Kalli K, et al. Distributed polymer optical fiber sensors: a review and outlook[J]. Photonics Research, 2021, 9(9): 1719-1733.

[10] Wu S N, Yan G F, Zhou B, et al. Open-cavity Fabry-Perot interferometer based on etched side-hole fiber for microfluidic sensing[J]. IEEE Photonics Technology Letters, 2015, 27(17): 1813-1816.

[11] Tian J J, Lu Y J, Zhang Q, et al. Microfluidic refractive index sensor based on an all-silica in-line Fabry-Perot interferometer fabricated with microstructured fibers[J]. Optics Express, 2013, 21(5): 6633-6639.

[12] Liu L, Ning T G, Zheng J J, et al. High-sensitivity strain sensor implemented by hybrid cascaded interferometers and the Vernier-effect[J]. Optics & Laser Technology, 2019, 119: 105591.

[13] Wen X Y, Lin G H, Jia X N, et al. Modal interference discrepancy and its application to a modified fiber Mach-Zehnder Vernier interferometer[J]. Optics Express, 2022, 30(24): 42875-42891.

[14] 刘福禄, 张钰民, 庄炜, 等. 基于游标效应和基底增敏的复合光纤结构温度传感器[J]. 光学学报, 2021, 41(15): 1506002.
Liu F L, Zhang Y M, Zhuang W, et al. Fiber temperature sensor with composite structure based on vernier effect and substrate sensitization[J]. Acta Optica Sinica, 2021, 41(15): 1506002.

[15] 胡白燕, 文富荣, 程永山, 等. 基于级联腔法布里-珀罗干涉仪的温度和压力同时测量[J]. 激光与光电子学进展, 2021, 58(19): 1906006.
Hu B Y, Wen F R, Cheng Y S, et al. Simultaneous measurement of temperature and pressure based on cascaded Fabry-Perot interferometer[J]. Laser & Optoelectronics Progress, 2021, 58(19): 1906006.

[16] 胡白燕, 文富荣, 程永山, 等. 基于级联腔法布里-珀罗干涉仪的温度和压力同时测量[J]. 激光与光电子学进展, 2021, 58(19): 1906006.
Hu B Y, Wen F R, Cheng Y S, et al. Simultaneous measurement of temperature and pressure based on cascaded Fabry-Perot interferometer[J]. Laser & Optoelectronics Progress, 2021, 58(19): 1906006.

[17] Li J W, Zhang M, Wan M G, et al. Ultrasensitive refractive index sensor based on enhanced Vernier effect through cascaded fiber core-offset pairs[J]. Optics Express, 2020, 28(3): 4145-4155.

[18] Gomes A D, Bartelt H, Frazão O. Optical vernier effect: recent advances and developments[J]. Laser & Photonics Reviews, 2021, 15(7): 2000588.

[19] Zhou C, Zhou Q, Wang B, et al. High-sensitivity relative humidity fiber-optic sensor based on an internal-external Fabry-Perot cavity Vernier effect[J]. Optics Express, 2021, 29(8): 11854-11868.

[20] 赵玉欣, 姜久兴, 杨玉强, 等. 基于游标效应增敏的全光纤液体折射率传感器[J]. 光子学报, 2019, 48(11): 1148022.
Zhao Y X, Jiang J X, Yang Y Q, et al. A sensitivity-enhanced all-fiber-optic liquid refractive index sensor based on vernier effect[J]. Acta Photonica Sinica, 2019, 48(11): 1148022.

[21] Zhang J, Liao H, Lu P, et al. Ultrasensitive temperature sensor with cascaded fiber optic Fabry-Perot interferometers based on vernier effect[J]. IEEE Photonics Journal, 2018, 10(5): 6803411.

[22] Qi K Y, Zhang Y D, Sun J F, et al. Fiber bending sensor with turning point in a multimode fiber peanut-like structure[J]. IEEE Sensors Journal, 2022, 22(8): 7772-7778.

[23] Sun X T, Gong H P, Xie M Y, et al. All-fiber humidity sensor based on Michelson interferometer with hyaluronic acid and polyvinyl alcohol composite film[J]. Optical Fiber Technology, 2020, 60: 102381.

[24] Shao M, Sun H N, Liang J J, et al. In-fiber Michelson interferometer in photonic crystal fiber for humidity measurement [J]. IEEE Sensors Journal, 2021, 21(2): 1561-1567.

[25] Shao M, Zhang R, Gao H, et al. A high-sensitivity low-temperature sensor based on Michelson interferometer in seven-core fiber[J]. IEEE Photonics Technology Letters, 2021, 33(23): 1293-1296.

[26] Shao M, Zhang R, Zhao X, et al. Dual-core fiber based in-line Michelson interferometer for humidity sensing[J]. Optical Fiber Technology, 2021, 64: 102570.

[27] Liao H, Lu P, Fu X, et al. Sensitivity amplification of fiber-optic in-line Mach-Zehnder Interferometer sensors with modified Vernier-effect[J]. Optics Express, 2017, 25(22): 26898-26909.

[28] Xie L Q, Sun B, Chen M M, et al. Sensitivity enhanced temperature sensor with serial tapered two-mode fibers based on the Vernier effect[J]. Optics Express, 2020, 28(22): 32447-32455.

[29] 彭石军. 基于SMS光纤结构器件及其应用研究[D]. 哈尔滨: 哈尔滨工程大学, 2012: 38-40.
Peng S J. Research on optical fiber structure device based on SMS and its application[D]. Harbin: Harbin Engineering University, 2012: 38-40.

[30] Zong S Y, Wen X Y, Li M, et al. Multiple interference components in a fiber Mach - Zehnder interferometer sensor and their influence on wavelength shift tracing[J]. Measurement Science and Technology, 2021, 32(3): 035118.

[31] Choi H Y, Kim M J, Lee B H. All-fiber Mach-Zehnder type interferometers formed in photonic crystal fiber[J]. Optics Express, 2007, 15(9): 5711-5720.

[32] Yu X J, Bu D, Chen X F, et al. Lateral stress sensor based on an in-fiber Mach-Zehnder interferometer and Fourier analysis[J]. IEEE Photonics Journal, 2016, 8(2): 6801710.

Few-Mode Fiber Mode Reflection Michelson Interferometer and Its Vernier Sensitization Application

Wu Ruini[1], Lin Guohui[2], Lü Haifei[1], Li Min[1], Li Mingyu[1], Wang Jiafu[1], Wen Xiaoyan[1*]

[1]*School of Science, Wuhan University of Technology, Wuhan* 430070, *Hubei, China*;

[2]*Wireless Product Operation Division, ZTE Corporation, Shenzhen* 518000, *Guangdong, China*

Abstract

Objective Refractive index (RI) is one of the most important parameters to guide light and control light-matter interaction. Recently optical fiber RI sensors have attracted great attention in various areas such as physics, photonics, chemistry, biology, and environment monitoring due to their remote on-line sensing. The optical Vernier effect produced by the cascade of two interferometers with close free spectral ranges (FSRs) has been developed to improve the sensitivity of RI sensors. The wavelength shift of the spectral envelope of the cascaded sensors is much larger than that of the unit sensing interferometer when the environmental refractive index is changed. FSRs of the two unit interferometers, determined by the interferometer′s cavity lengths, should be carefully designed and calibrated to improve sensitization fold as much as possible. Additionally, both of the two unit interferometers should have high fringe visibility and stable interference components for obtaining obvious cascaded spectral envelopes. Till now, the most reported unit interferometer for Vernier sensitization is the Fabry-Perot interferometer (FPI). Unfortunately, the fabrication of an FPI interferometer requires complicated fiber alignment and fine cavity length adjustment, which leads to poor reproducibility in the sensor fabrication. Michelson interferometer (MI) can also be employed as a unit interferometer for Vernier sensitization. Those traditional MI unit interferometers usually include multi-mode fiber, twin core fiber, and coreless fiber. In the aforementioned fibers, multiple cladding modes are inevitably stimulated and multiple modal interference are involved in the spectrum of the cascaded sensor. As a result, interference component analysis of the spectrum is complex. In addition, controllable stimulation of these modes is difficult. Few-mode fiber (FMF) could only support the transmission of limited modes. The decreased mode quantity leads to a simple interference component, which is beneficial to the sensor cascade. The interference component in an FMF-based MI is stable since all the modes in FMF are confined in the fiber core and immune to environmental refractive index changes. Meanwhile, MI could be naturally formed by the two end faces of a single FMF, without the necessity for fiber alignment and fine cavity length adjustment. Thus, FMF-based MI is a good candidate for reference interferometers in Vernier sensors. In this study, an FMF-based MI-FPI Vernier sensor has been developed for RI sensitization. FPI acts as a sensing interferometer because of its open cavity, and MI made from an FMF serves as the reference interferometer due to its simple interference component and stable interference spectrum. Due to FMF and MI, the dual cavity mismatching problem and poor controllability of traditional dual FPI sensors could be solved.

Methods For the proposed FMF-based MI-FPI sensor, MI is implemented by fusing an incident single-mode fiber (SMF) with an FMF in a certain core-offset, and FPI is formed by the cavity sandwiched between the free end face of the FMF and one of the end face of an another SMF. Both FMF and the two SMFs are fixed on a slide by UV glue. The interference spectrum of the FMF-based MI is mainly affected by two structural parameters including the offset between incident SMF and FMF, and the FMF length. Offset fusion will induce asymmetrical optical mode field distribution in fiber and excite the specific mode. Thus, the influence of core-offset distance between SMF and FMF on mode excitation efficiency, and the effect of FMF length on the Vernier sensitization effect are simulated. Moreover, a virtual MI is developed to analyze the Vernier enhancement effect on unit FPI to provide theoretical guidance for the FMF length selection. The interference component in the cascaded structure is analyzed by taking a fast Fourier transform (FFT) of the experimental spectrum. Due to FFT, the spatial frequency of a certain interference component can be ascertained, and based on simulation data the cascaded MI-FPI sensor is fabricated. The sensor fabrication is as follows. Firstly, an FMF-based MI with the FMF length of 32.4 cm and the core-offset of 3 μm is fabricated. Then, an FPI is formed by gradually drifting another SMF to the end face of the FMF. Both FMF and the two SMFs are fixed on a slide by UV glue. The interference spectrum of the fabricated MI-FPI sensor is recorded by an optical spectrum analyzer (YOKOGAWA, AQ6370) with a resolution of 0.02 nm. A super-luminescent light-emitting diode (SLED) with a wavelength range from 1500-1600 nm is adopted as the light resource. For RI measurement, NaCl solutions with different RI in a range of 1.3384-1.3412 are employed and the RI of each NaCl solution is determined by an Abbe refractometer.

Results and Discussions Refractive index response sensitivity of the cascaded MI-FPI sensor is measured to be

12466.956 nm/RIU in the range of 1.3384-1.3412, which is 12.29 times enhanced over the FPI sensor without MI cascade. The amplification limit and the influence factors are analyzed, and the sensitization limit of the sensor is determined by the ratio of $\xi_S/|\xi_R-\xi_S|$. Thus the sensor sensitivity could be further improved in the following two ways. One is to adopt a light source with a wider spectrum to decrease $|\xi_R-\xi_S|$, and the other is to raise the FPI cavity to increase ξ_S. The experimentally measured magnification factor slightly deviates from the theoretical one. The possible reasons are discussed. Firstly, followed by inverse Fourier transform, a frequency filtering method is utilized, which is suitable for analyzing cosine signals. However, since the spectrum of the experimental MI is not a regular cosine spectrum, the FSR at short wavelengths is smaller than that at long wavelengths, leading to a deviation between the experimentally measured magnification factor and the theoretical one. Secondly, during the experiment, there are small errors in the length control of FMF and FPI, which is the cavity length of MI (L_R) and FPI (L_S), also resulting in certain deviation of the magnification factor.

Conclusions A refractive index Vernier sensor based on an FMF-MI is developed. The sensor consists of an MI serving as the reference unit interferometer and an FPI serving as the sensing unit interferometer. Experimental results show that the MI-FPI sensor has a refractive index sensitivity of 12466.956 nm/RIU in the range of 1.3384-1.3412, which is 12.29 times improved compared with the FPI sensor without MI cascade. The proposed MI-FPI sensor is characterized by high sensitivity, simple fabrication, and sound reproducibility. Therefore, it can be a suitable choice for various applications in biological and chemical fields. Furthermore, the FMF-based MI has the unique advantages of simple structure, high extinction ratio, excellent stability, and mode controllability, which is suitable to be employed as a reference interferometer cascaded with other interferometers to achieve the Vernier effect.

Key words fiber optics; Michelson interferometer; few-mode fiber; mode reflection; Vernier effect; refractive index sensor